1

CASTOR3D: linear magnetohydrodynamics and diamagnetic drift effects

E. Strumberger [1],†, S. Günter[1], K. Lackner[1] and J. Puchmayr [1]

[1]Max Planck Institute for Plasma Physics, Boltzmannstr. 2, 85748 Garching, Germany

We upgrade the three-dimensional linear stability CASTOR3D code by taking into account gyro-viscosity in the momentum equation, as well as pressure and Hall terms in Ohm's law. Making use of the drift approximation, the resulting simplified version of Ohm's law is implemented. The ion and electron diamagnetic drift effects described by these newly implemented terms are investigated for ideal and resistive, low- and medium-n internal modes depending on the ratio of ion and electron pressures, and plasma resistivity. Stability studies are performed for two- and three-dimensional test equilibria. The results confirm previous findings, and provide new insights especially in the case of the three-dimensional equilibrium (e.g. reduction of the coupling of toroidal harmonics).

Key words: fusion plasma, plasma instabilities

---

1. Introduction

The stability properties of ideal and resistive modes are strongly influenced by kinetic effects (diamagnetic effects, viscosity, etc.). However, these effects are not included in the widely used simplified ideal or resistive fluid moment equations. Expressing the kinetic effects in terms of low-order fluid moments and including them in the fluid moment equations, the resulting extended equations describe both fluid and kinetic features (Chang & Callen 1992). Depending on the plasma properties, various sets of fluid equations (Mikhailovskii 1998; Huysmans *et al.* 2001; Schnack *et al.* 2006; Aiba 2016) and approximations of viscous stress tensor $\nabla \cdot \Pi$ and heat flux $\boldsymbol{q}$ (Chang & Callen 1992) have been established within the framework of magnetohydrodynamics (MHD). Drift MHD equations are used in linear (e.g. MISHKA-D (Huysmans *et al.* 2001), MISHKA-F (Chapman *et al.* 2006), MINERVA-DI (Aiba 2016)) and nonlinear (e.g. JOREK (Hoelzl *et al.* 2021), XTOR-2F (Lütjens & Luciani 2010)) codes to investigate diamagnetic drift effects. These codes differ in the applied numerical methods and in the detailed form of the extended MHD equations.

We upgrade the three-dimensional (3-D) linear resistive stability CASTOR3D code (Strumberger & Günter 2017, 2019) by taking into account gyro-viscosity in the momentum equation, as well as pressure and Hall terms in Ohm's law. Including additional

---

† Email address for correspondence: erika.strumberger@ipp.mpg.de

physical effects in linear MHD equations may lead to so-called 'parasitic' solutions which make it difficult to find and identify physically meaningful solutions. Besides a high numerical accuracy (high-quality equilibrium input, radial resolution, etc.) the analytical reduction of the model offers a possibility to reduce the occurrence of 'parasitic' modes (Schnack *et al.* 2006). We therefore make use of the drift approximation and implement the resulting simplified version of Ohm's law. This reduces the numerical problems and eliminates the Whistler waves.

The ion and electron diamagnetic drift effects caused by the newly implemented terms are investigated for ideal and resistive, low- and medium-n internal modes of two-dimensional (2-D) and 3-D high-β and 2-D low-β test equilibria. The types of these modes are specified more precisely by analysing the corresponding ideal or resistive energy functional that is determined from the solution of the eigenvalue problem without diamagnetic drift effects (Puchmayr, Dunne & Strumberger 2022). The diamagnetic drift effects are studied for ideal modes of the axisymmetric high-β equilibrium and resistive modes of the corresponding low-β equilibrium. The obtained results confirm the previous finding that diamagnetic drift effects may damp or even stabilise the modes (e.g. Aiba 2016). Moreover, we investigate the diamagnetic drift effects depending on various ratios of ion and electron pressures. The results indicate that the often used assumptions $p_i = p_e$ (equal pressures) or $p = p_e, p_i = 0$ (cold ions) (e.g. Lütjens & Luciani 2010; Aiba 2016; Pamela *et al.* 2020) may not always be a good approximation.

Usually, 3-D linear stability codes (e.g. CAS3D (Nührenberg 1996), TERPSICHORE (Anderson *et al.* 1990), etc.) are restricted to purely ideal stability studies. The CASTOR3D code, however, is a 3-D linear stability code which takes into account important physical effects just as 2-D linear stability codes (e.g. MARS (Chu *et al.* 1995), MISHKA-D (Huysmans *et al.* 2001), MISHKA-F (Chapman *et al.* 2006), MINERVA-DI (Aiba 2016), etc.). Considering a 3-D high-β test equilibrium with helical core, we investigate the ion diamagnetic drift effect on low-n^* internal modes, with n^* indicating the global mode structure. In many cases n^* corresponds to the dominant toroidal Fourier harmonic contributing to the mode (Strumberger & Günter 2019). The results are compared with those obtained for the corresponding axisymmetric equilibrium.

In §2 we present the extended MHD equations (§2.1) and their linearised forms which have been implemented in the CASTOR3D code (§2.2). The diamagnetic drift effects of these additional terms are investigated for ideal internal modes (§3.1) and resistive internal modes (§3.2) of the corresponding axisymmetric equilibria. Stability studies for the ideal internal modes of the 3-D equilibrium are the subject of §3.3. In §4 a summary of the results and an outlook on further studies are given. Finally, a simplified computation of the drift frequencyand a discussion of the numerical accuracy of the CASTOR3D results are presented in Appendices A and B, respectively.

2. Theory

2.1. *Extended MHD equations*

The upgraded version of the linear stability CASTOR3D code, which is used for the presented computations, is based on the extended MHD equations (Schnack *et al.* 2006):

$$\frac{\partial \rho}{\partial t} + V \cdot \nabla \rho + \rho \nabla \cdot V = 0, \tag{2.1}$$

$$\rho \frac{\partial V}{\partial t} + \rho (V \cdot \nabla) V = -\nabla p - \nabla \cdot \Pi + j \times B, \tag{2.2}$$

$$\frac{\partial T}{\partial t} + V \cdot \nabla T + (\Gamma - 1)T\nabla \cdot V = 0, \tag{2.3}$$

$$E + V \times B + \frac{m_i}{e\rho}\nabla p_e = \frac{m_i}{e\rho}j \times B + \eta j. \tag{2.4}$$

They correspond to the generally used single-fluid equations (e.g. Huysmans, Goedbloed & Kerner 1993) plus additional two-fluid terms. These equations are derived from the two-fluid MHD equations (Braginskii 1965) making several assumptions and approximations, e.g. assuming quasi-neutrality $n = n_i = n_e$ (n_i is ion density, n_e is electron density), neglecting the electron mass ($m_i >> m_e$, mass density $\rho = m_i n + m_e n \approx m_i n$), using pressure $p = p_i + p_e = n(T_i + T_e) = nT$ (T_i is ion temperature, T_e is electron temperature, $T = T_i + T_e$) and making the velocity approximation $V = m_i V_i + m_e V_e / m_i + m_e \approx V_i$, with V_i being the ion velocity. The set of equations is closed with the Maxwell equations

$$\nabla \cdot E = 0, \quad \nabla \times E = -\frac{\partial B}{\partial t}, \quad \nabla \times B = \mu_0 j, \quad \nabla \cdot B = 0 \tag{2.5a-d}$$

(E is electric field, B is magnetic field, j is current density), where $\mu_0 \epsilon_0 (\partial E / \partial t)$ is neglected. The ion velocity V_i is given by

$$V_i = \underbrace{\frac{E \times B}{B^2}}_{=V_E} + \underbrace{V \cdot \frac{B}{B}}_{=V_{||}} + \underbrace{\alpha \frac{1}{\rho}\frac{B \times \nabla p_i}{B^2}}_{=V_i^*} \cdots. \tag{2.6}$$

There, $V_{\mathrm{MHD}} = V_E + V_{||}$ is the so-called MHD velocity, V_i^* is the ion diamagnetic drift velocity and $\alpha = m_i/e$, with e being the elementary charge. Additionally to the ideal MHD equations, the extended MHD equations take into account the viscous force density $-\nabla \cdot \Pi$ in the momentum equation (2.2), as well as the electron pressure-gradient term $(m_i/e\rho)\nabla p_e$, the Hall term $(m_i/e\rho)j \times B$ and the plasma resistivity term ηj in the extended Ohm's law (2.4). The viscous stress tensor Π splits into $\Pi = \Pi_{||} + \Pi_{\wedge} + \Pi_{\perp}$, with parallel $\Pi_{||}$, cross (gyro-viscous) $\Pi_{\wedge}$, and perpendicular $\Pi_{\perp}$ parts. We already introduced the approximation

$$-\nabla \cdot \Pi_{||} = \mu_{||}\Delta_{||}V \tag{2.7}$$

in the previous CASTOR3D version (Strumberger & Günter 2019), while the perpendicular viscosity is not implemented in the code. The parallel viscosity coefficient $\mu_{||}$ is an input parameter. However, in this work we neglect the parallel viscosity ($\mu_{||} = 0$), and concentrate our studies on the diamagnetic drift effects. The gyro-viscous force is approximated by (Chang & Callen 1992)

$$-\nabla \cdot \Pi_{\wedge} \approx \rho(V_i^* \cdot \nabla)V. \tag{2.8}$$

This expression is generally known as gyro-viscous cancellation. Using (2.7) and (2.8), the momentum equation (2.2) reduces to

$$\rho\frac{\partial V}{\partial t} + \rho((V - V_i^*) \cdot \nabla)V = -\nabla p + \mu_{||}\nabla_{||}V + j \times B. \tag{2.9}$$

The extended Ohm's law (2.4) is simplified by using the drift approximation of the Hall term (Schnack *et al.* 2006):

$$\nabla_{\perp}p \approx j \times B, \tag{2.10}$$

which leads to

$$\mathbf{E} + \mathbf{V} \times \mathbf{B} + \frac{\alpha}{\rho}\nabla_{\parallel}p_e - \frac{\alpha}{\rho}\nabla_{\perp}p_i = \eta\mathbf{j} \tag{2.11}$$

and eliminates the Whistler waves.

As already mentioned, single-fluid codes that include two-fluid effects often use the assumption $p_i = p_e = 0.5p$, that is, $T_i = T_e$. However, measured ion and electron temperatures may be different. Therefore, we use the ansatz

$$p_i = \alpha_T p, \quad p_e = (1 - \alpha_T)p, \tag{2.12a,b}$$

with $0 \leq \alpha_T \leq 1$. The parameter α_T provides an additional degree of freedom that allows one to choose a more realistic ratio of ion and electron pressures with respect to the measured temperatures, that is, a more realistic treatment of ion and electron diamagnetic drift effects. Application of (2.12a,b) to the ion drift velocity (2.6) and the pressure terms of (2.11) yields

$$V_i^* = \alpha\alpha_T\frac{1}{\rho}\frac{\boldsymbol{B} \times \boldsymbol{\nabla}p}{B^2} \tag{2.13}$$

and the simplified Ohm's law

$$\boldsymbol{E} + \boldsymbol{V} \times \boldsymbol{B} + \frac{\alpha}{\rho}\nabla_{\parallel}p - \frac{\alpha\alpha_T}{\rho}\boldsymbol{\nabla}p = \eta\boldsymbol{j}, \tag{2.14}$$

with $\nabla_{\parallel}p = (1/B^2)\boldsymbol{B}(\boldsymbol{B} \cdot \boldsymbol{\nabla}p)$.

Equations (2.1), (2.9), (2.3) and (2.14) of the standard drift model are only valid in the drift ordering, that is, $\epsilon \sim \delta^2$ and $\xi \sim \delta$ with $\epsilon = \omega/\Omega_i$ (ω is characteristic frequency, Ω_i is ion gyro-frequency), $\xi = V_0/V_{thi}$ (V_0 is characteristic flow velocity, V_{thi} is ion thermal speed) and $\delta = \rho_i/L$ (ρ_i is ion Larmor radius, L is macroscopic scale length) (Schnack *et al.* 2006).

2.2. *Linearisation of the extended MHD equations*

In order to fulfil $\boldsymbol{\nabla} \cdot \boldsymbol{B} = 0$, we use $\boldsymbol{B} = \boldsymbol{\nabla} \times \boldsymbol{A}$ ($\boldsymbol{A}$ is magnetic vector potential), while the Weyl gauge (electric scalar potential $\Phi_E = 0$) yields $\boldsymbol{E} = -(\partial\boldsymbol{A}/\partial t)$. The time dependence of the perturbed quantities is assumed to be $\sim e^{\lambda t}$ with $\lambda = \gamma + i\omega$ (γ is growth rate, ω is oscillation frequency of the mode). Using the ansatz $f(\boldsymbol{r}, t) = f_0(\boldsymbol{r}) + e^{\lambda t}f_1(\boldsymbol{r})$ for ρ, T, $\boldsymbol{V}$ and $\boldsymbol{A}$, the linearised forms of the extended fluid equations (2.1), (2.9), (2.3) and (2.14) read

$$\lambda\rho_1 = -\boldsymbol{V}_0 \cdot \boldsymbol{\nabla}\rho_1 - \boldsymbol{V}_1 \cdot \boldsymbol{\nabla}\rho_0 - \rho_1\boldsymbol{\nabla} \cdot \boldsymbol{V}_0 - \rho_0\boldsymbol{\nabla} \cdot \boldsymbol{V}_1, \tag{2.15}$$

$$\begin{aligned}
\rho_0\lambda\boldsymbol{V}_1 = &-\rho_1(\boldsymbol{V}_0 \cdot \boldsymbol{\nabla})\boldsymbol{V}_0 - \rho_0(\boldsymbol{V}_1 \cdot \boldsymbol{\nabla})\boldsymbol{V}_0 - \rho_0(\boldsymbol{V}_0 \cdot \boldsymbol{\nabla})\boldsymbol{V}_1 \\
&+\rho_1(\boldsymbol{V}_{i0}^* \cdot \boldsymbol{\nabla})\boldsymbol{V}_0 + \rho_0(\boldsymbol{V}_{i1}^* \cdot \boldsymbol{\nabla})\boldsymbol{V}_0 + \rho_0(\boldsymbol{V}_{i0}^* \cdot \boldsymbol{\nabla})\boldsymbol{V}_1 \\
&-\frac{1}{m_i}\boldsymbol{\nabla}(\rho_0 T_1) - \frac{1}{m_i}\boldsymbol{\nabla}(T_0\rho_1) + \mu_{\parallel}\Delta_{\parallel}\boldsymbol{V}_1 \\
&+\frac{1}{\mu_0}(\boldsymbol{\nabla} \times (\boldsymbol{\nabla} \times \boldsymbol{A}_1)) \times (\boldsymbol{\nabla} \times \boldsymbol{A}_0) \\
&+\frac{1}{\mu_0}(\boldsymbol{\nabla} \times (\boldsymbol{\nabla} \times \boldsymbol{A}_0)) \times (\boldsymbol{\nabla} \times \boldsymbol{A}_1), \tag{2.16}
\end{aligned}$$

$$\lambda T_1 = -\boldsymbol{V}_1 \cdot \boldsymbol{\nabla}T_0 - \boldsymbol{V}_0 \cdot \boldsymbol{\nabla}T_1 - (\Gamma - 1)T_1\boldsymbol{\nabla} \cdot \boldsymbol{V}_0 - (\Gamma - 1)T_0\boldsymbol{\nabla} \cdot \boldsymbol{V}_1, \tag{2.17}$$

$$\frac{\partial \boldsymbol{A}_1}{\partial t} = \boldsymbol{V}_1 \times \boldsymbol{B}_0 + \boldsymbol{V}_0 \times (\nabla \times \boldsymbol{A}_1) + \frac{\alpha}{\rho_0} \frac{1}{B_0^2} \boldsymbol{B}_0 \left((\nabla \times \boldsymbol{A}_1) \cdot \frac{1}{m_i} \nabla(\rho_0 T_0) \right)$$

$$+ \frac{\alpha}{\rho_0} \frac{1}{B_0^2} \boldsymbol{B}_0 \left(\boldsymbol{B}_0 \cdot \frac{1}{m_i} \nabla(\rho_1 T_0 + \rho_0 T_1) \right) - \alpha \alpha_T \frac{1}{\rho_0} \frac{1}{m_i} \nabla(\rho_1 T_0 + \rho_0 T_1)$$

$$+ \alpha \alpha_T \frac{\rho_1}{\rho_0^2} \frac{1}{m_i} \nabla(\rho_0 T_0) - \frac{\eta}{\mu_0} (\nabla \times (\nabla \times \boldsymbol{A}_1)). \tag{2.18}$$

Here $\rho_0, \boldsymbol{V}_0, T_0$ and $\boldsymbol{A}_0$ are the equilibrium quantities of density, ion velocity (2.6), temperature ($T_0 = T_{0e} + T_{0i}$) and magnetic vector potential, while $\rho_1, \boldsymbol{V}_1, T_1$ and $\boldsymbol{A}_1$ are their perturbations. The perturbation of the ion diamagnetic drift velocity reads

$$\boldsymbol{V}_{i1}^* = -\alpha \alpha_T \frac{\rho_1}{\rho_0^2} \frac{\boldsymbol{B}_0 \times \nabla p_0}{B_0^2} + \alpha \alpha_T \frac{1}{\rho_0} \frac{\boldsymbol{B}_0 \times (T_0 \nabla \rho_1 + T_1 \nabla \rho_0 + \rho_0 \nabla T_1 + \rho_1 \nabla T_0)}{B_0^2}$$

$$+ \alpha \alpha_T \frac{1}{\rho_0} \frac{(\nabla \times \boldsymbol{A}_1) \times \nabla p_0}{B_0^2} - 2\alpha \alpha_T \frac{1}{\rho_0} \frac{\boldsymbol{B}_0 \cdot (\nabla \times \boldsymbol{A}_1)}{B_0^4} (\boldsymbol{B}_0 \times \nabla p_0). \tag{2.19}$$

The corresponding boundary conditions and boundary terms of the linearised MHD equations are not affected by the newly implemented terms. They are described in detail in previous works (e.g. Huysmans *et al.* 1993; Strumberger & Günter 2017, 2019).

3. Stability studies

The linearised, extended MHD equations (2.15)–(2.18) are implemented in the CASTOR3D code in general 3-D formulation. This general formulation allows one to use various flux coordinate types (Strumberger & Günter 2017) (see also Appendix B). The parameter $\alpha = m_i/e$ is implemented in the form $\alpha = \alpha_s(m_i/e)$, with $0 \le \alpha_s \le 1$ being a scaling parameter. The latter allows the modification of the strength of the diamagnetic drift effects. This parameter is mainly necessary for computational reasons. Increasing α_s step by step may lead from a growth rate without diamagnetic drift effects to a growth rate that is strongly reduced by these effects, or even to a stable solution. Certainly, only $\alpha_s = 0$ and $\alpha_s = 1$ yield physically relevant solutions.

Stability studies are performed for test equilibria assuming the following conditions: circular cross-section, minor radius $a = 1$ m, aspect ratio $A = 1.6$, flat rotational transform profile (axis value $\iota_a = 1.01$, boundary value $\iota_b = 0.63$) and pressure profile defined by an analytical function $p(s) = p_a(1 - 2s^2 + s^4)$, with radial coordinate s being the square root of the normalised toroidal flux. In figure 1(*a*) we show the rotational transform profile ι, the normalised pressure profile p_N and the chosen normalised profiles of ion density n_N (deuterons) and temperature T_N. We study the diamagnetic drift effects for an axisymmetric high-β (volume-averaged plasma β: $\langle \beta \rangle = 2.97\%$) equilibrium and a low-$\beta$ ($\langle \beta \rangle = 0.97\%$) equilibrium, and a 3-D high-β ($\langle \beta \rangle = 2.97\%$) equilibrium with an $n = 1$ helical core (see figure 1*b*). The latter is the result of a 3-D fixed-boundary equilibrium calculation with axisymmetric plasma boundary (Strumberger & Günter 2017). All equilibria are computed with the 3-D NEMEC code (Hirshman & Whitson 1983; Hirshman, van Rij & Merkel 1986). Ion and electron diamagnetic drift effects are investigated for various ratios of ion and electron pressures. We choose these simple test equilibria, because they are ideal and resistive unstable with respect to low- and medium-n internal modes, and they are numerically easy to handle. Due to their simple geometry and very flat q-profile ($q = 1/\iota$) only few poloidal and toroidal (3-D case) harmonics couple together. The resulting eigenvalue problems are, therefore, fast to solve, and allow detailed physical and numerical parameter studies.
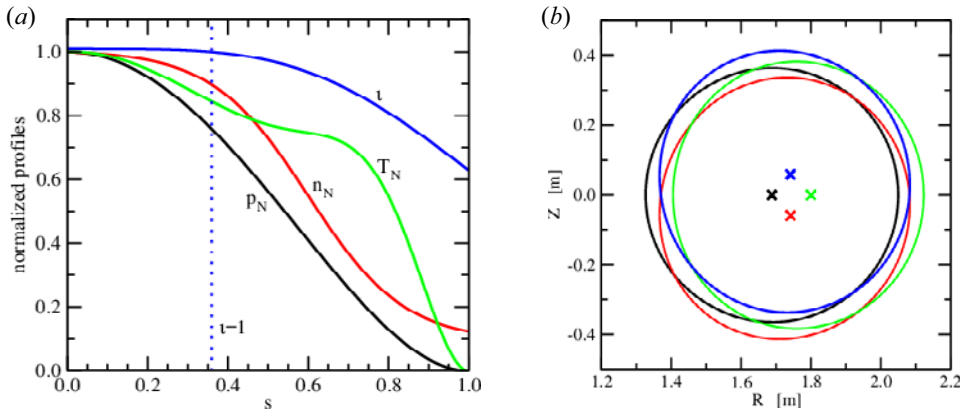
FIGURE 1. (a) Rotational transform profile ι and normalised profiles of pressure p_N, ion density n_N and temperature T_N as functions of the square root of the normalised toroidal flux s. The dotted vertical line marks the position of the $\iota = 1$ rational flux surface. (b) Helical core of the 3-D equilibrium: $\iota = 1$ flux surface and position of the magnetic axis (crosses) at the toroidal cross-sections $\varphi = 0°$, $90°$, $180°$ and $270°$.
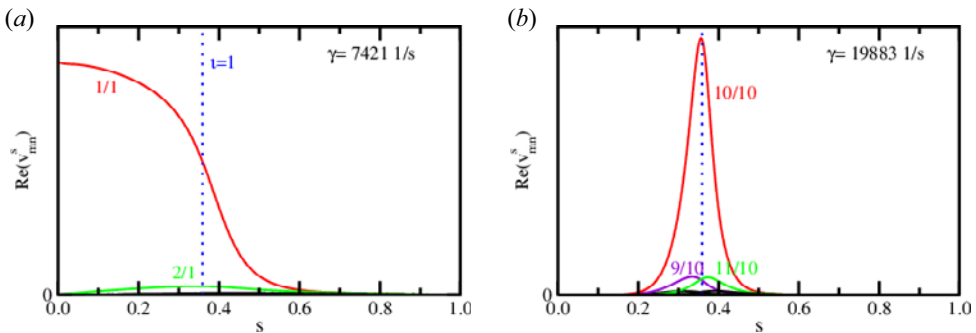

FIGURE 2. Fourier spectra of the real part of the radial velocity perturbation for (a) an $n = 1$ and (b) an $n = 10$ mode. The dotted vertical line indicates the position of the $\iota = 1$ flux surface.

3.1. Ideal stability studies (2-D equilibrium)

We study the stability of an axisymmetric high-β equilibrium (pressure $p_a = 33.75\,\text{kPa}$, deuteron ion density $n_a = 0.7 \times 10^{20}\,\text{m}^{-3}$ and temperature $T_a = 3009\,\text{eV}$ at the magnetic axis) with equilibrium ion velocity $V_{i0} = 0$, that is, we assume that the contributions to the ion velocity (2.6) are either zero or cancel. This equilibrium is unstable with respect to ideal modes localised at the $\iota = 1$ rational flux surface. Using 2-D straight field line coordinates, the characteristic Fourier spectra of the real part of the radial velocity perturbation are shown for the $n = 1$ and $n = 10$ modes in figures 2(a) and 2(b).

Recently, the diagnostic part of the CASTOR3D code has been extended by implementing the calculation of the resistive energy functional from the solution of the eigenvalue problem (Puchmayr et al. 2022). This energy functional provides information on the different energetic drives of ideal and resistive modes. The energy of the perturbations is decomposed into stabilising contributions δW_{STA}, the pressure-gradient drive δW_{DP} and the parallel current-density drive δW_{CUR}. For easy comparison of the energy across different perturbations, the energy values are normalised as described
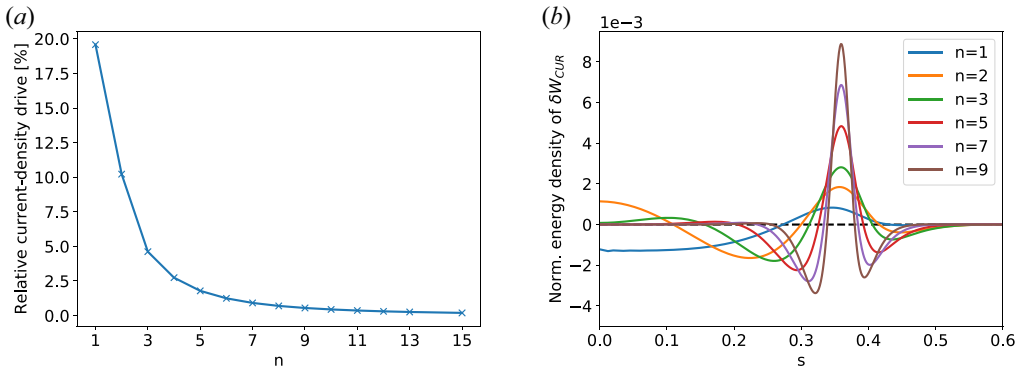
FIGURE 3. Energetic decomposition of the ideal internal perturbations of the considered high-β equilibrium. (*a*) Relative current-density drive as a function of the toroidal mode number and (*b*) normalised energy density corresponding to the current-density drive as a function of the square root of the normalised toroidal flux.

in Puchmayr *et al.* (2022), and we define the relative current-density drive as $\delta W_{\text{CUR}}/(\delta W_{\text{CUR}} + \delta W_{\text{DP}})$. The analysis of the ideal internal modes of the considered high-β equilibrium shows that these modes are mainly pressure-gradient-driven. With increasing toroidal mode number, the perturbations get increasingly localised at the $q = 1$ surface, where the equilibrium pressure gradient is high compared with that of the near-axis region, and become more pressure-gradient-driven. The $n = 1$ mode is the only mode that has a destabilising current density contribution at the magnetic axis, while the $n = 2$ mode has a stabilising one (see figure 3*b*). There, the finite contributions result from the $m = 1$ components of these two modes, while for the higher-n modes the $m = 1$ components are negligibly small at the magnetic axis. Furthermore, the integrated pressure-gradient drive δW_{DP} strongly increases with increasing toroidal mode number similarly to the resistive case shown in figure 7(*c*), while the integrated current-density drive δW_{CUR} remains small due to the cancellation of stabilising and destabilising radial regions. So, these modes are most probably ideal internal kink and interchange modes.

We now investigate the effects of ion and electron magnetic drift on those ideal modes depending on the toroidal mode number n. We determine the dominant effect by executing these computations for various ratios of the ion and electron pressures: (i) $p_i = p_e$, (ii) $p_i = \alpha_T p, p_e = (1 - \alpha_T)p$ with $\alpha_T = 0.4$ and (iii) $p_i = 0, p_e = p$ (cold ions). A large stabilising effect is observed for $p_i = p_e$ and $p_i = 0.4p$. The growth rates are reducedand the modes oscillate with negative frequencies. The modes are stabilised when the absolute value of the oscillation frequency $|\omega|$ of the mode exceeds the ideal growth rate, $|\omega| \gtrsim \gamma_{\text{ideal}}$. Therefore, the considered modes are stable for $p_i = 0.5p, n > 6$ and $p_i = 0.4p, n > 8$, as shown in figures 4(*a*) and 4(*b*) and verified in figures 4(*c*) and 4(*d*). Growth rates and oscillation frequencies are plotted as functions of the scaling parameter α_s in the latter two figures. There, the $n = 7$ and $n = 9$ modes stabilise for $p_i = 0.5p$, $\alpha_s \geq 0.9705$ and $p_i = 0.4p$, $\alpha_s \geq 0.9574$, respectively. The oscillation frequencies scale in good agreement with the toroidal mode number n (figure 4*a*,*b*) and the scaling parameter α_s (figure 4*c*,*d*). A small deviation from the linear increase of ω as function of α_s only appears close to stabilising α_s value when $|\omega|$ exceeds γ_{ideal}. Although the two considered pressure ratios do not differ much, there are significant differences in growth rates, oscillation frequencies and the lowest n values of the stable modes.
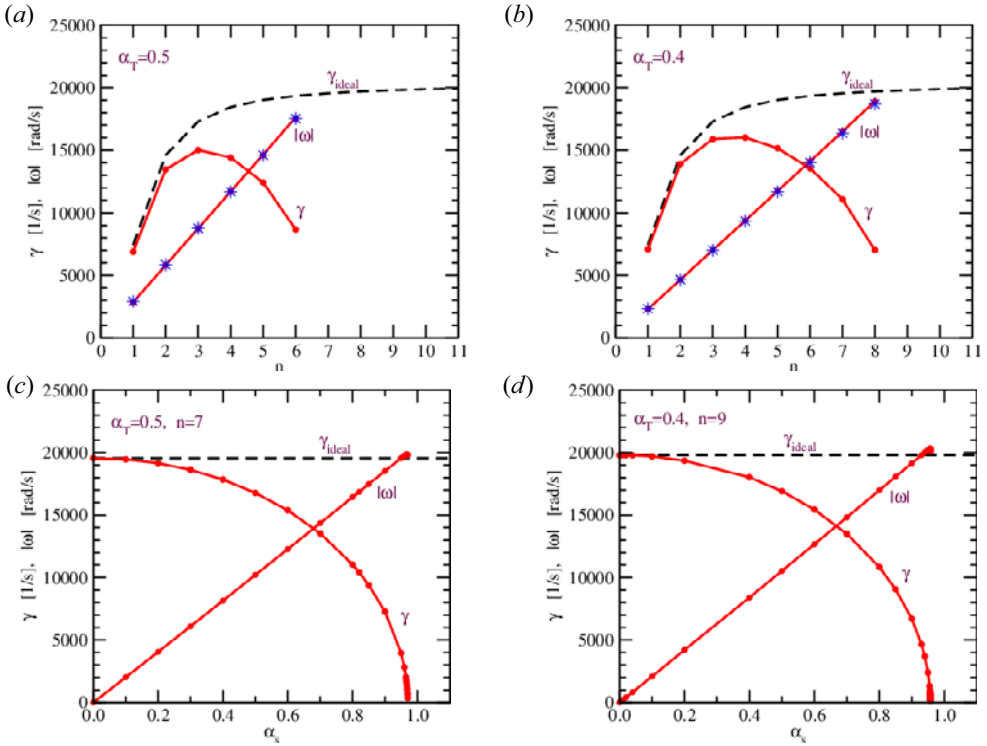
FIGURE 4. Assuming (a,c) $p_i = p_e = 0.5p$ and (b,d) $p_i = 0.4p$, $p_e = 0.6p$, growth rate γ and absolute value of the oscillation frequency $|\omega|$ are plotted (a,b) as functions of the toroidal mode number n and (c,d) as functions of the scaling parameter α_s for (c) the $n=7$ and (d) the $n=9$ modes. (a,b) The blue stars represent the absolute value of half of the ion diamagnetic drift frequency $|\omega_i^*|/2$ (A2). The black dashed lines mark the growth rates γ_{ideal} obtained without taking diamagnetic drift effects into account.

The obtained results are in good agreement with the results and the dispersion relation

$$\gamma + \mathrm{i}\omega = \mathrm{i}\frac{\omega_i^*}{2} \pm \sqrt{\gamma_{\text{ideal}}^2 - \left(\frac{\omega_i^*}{2}\right)^2} \tag{3.1}$$

presented in Aiba (2016), that is, the modes are marginally stable for $\gamma_{\text{ideal}} = \omega_i^*/2$. A simplified analytical expression of ω_i^* is presented in Appendix A. The resulting ion drift frequencies are $|\omega_i^*| = 5841\,\text{rad s}^{-1}$ ($p_i = 0.5p$) and $4673\,\text{rad s}^{-1}$ ($p_i = 0.4p$) for a 1/1 mode at the $\iota = 1$ flux surface. The calculated drift frequencies $|\omega_i^*|/2$ are compared with the oscillation frequencies of the modes in figures 4(a) and 4(b). They agree very well as stated by (3.1). Comparing the numerical results shown in figures 4(c) and 4(d) with the calculated drift frequencies, we obtain $\gamma_{\text{ideal}}(n=7) = 19\,556\,\text{rad s}^{-1} \approx |\omega| = 19\,805\,\text{rad s}^{-1} \approx \alpha_s|\omega_i^*|/2 = 19\,840\,\text{rad s}^{-1}$ and $\gamma_{\text{ideal}}(n=9) = 19\,804\,\text{rad s}^{-1} \approx |\omega| = 20\,082\,\text{rad s}^{-1} \approx \alpha_s|\omega_i^*|/2 = 20\,132\,\text{rad s}^{-1}$, respectively. Here the used expression (A2) is a good approximation for ω_i^*, because the Fourier spectra of the considered modes are dominated by only one poloidal harmonic (see figure 2). Besides, the ion diamagnetic drift is the dominant effect for these ideal modes, while the electron diamagnetic drift effect is negligible, as shown in figure 5. There, growth rate and oscillation frequency (marked by red crosses) are presented as functions of the toroidal mode number n for a
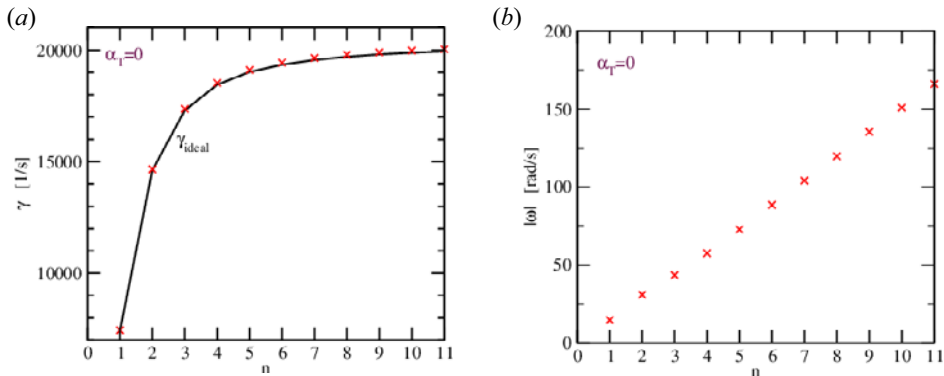
(*a*)

(*b*)

FIGURE 5. (*a*) Growth rate and (*b*) absolute value of the oscillation frequency ($\omega < 0$) as functions of the toroidal mode number n assuming cold ions ($\alpha_T = 0$) (red crosses). In (*a*) the black solid line marks the growth rate γ_{ideal} obtained without taking diamagnetic drift effects into account.

plasma with cold ions ($p_i = 0$). That is, there is no ion, but only an electron diamagnetic drift represented by the parallel electron pressure-gradient term in (2.11) (Yu, Günter & Scott 2003). Here, however, the latter has no stabilising effect, but an insignificant destabilising effect. It causes mode oscillations with frequencies increasing linearly with n, but which are negligibly small in comparison with the mode frequencies induced by the ion diamagnetic drift effect.

3.2. *Resistive stability studies (2-D equilibrium)*

We consider the same plasma configuration as for the ideal modes, but with a much lower plasma β of $\langle\beta\rangle = 0.97\,\%$ (pressure $p_a = 11.25$ kPa, deuteron ion density $n_a = 0.7 \times 10^{20}$ m^{-3} and temperature $T_a = 1004$ eV at the magnetic axis). Again, we assume that all contributions to the equilibrium ion velocity are either zero or cancel ($V_{i0} = 0$). This low-β equilibrium is also unstable with respect to internal modes located at the $\iota = 1$ flux surface. These modes show an analogous mode structure as the ideal modes considered in the previous section (compare figures 2*a*,*b* and 6*c*,*d*). However, they are only unstable for finite plasma resistivity η, and their slow growth rates approximately scale with $\eta^{1/3}$ as shown in figure 6(*b*) (we assume $\eta = $ constant). This scaling is typical for resistive kink and interchange modes.

Analysing the resistive energy functional of these modes highlights their pressure-gradient-driven character. Compared with the ideal modes of the high-β equilibrium, the resistive modes of the low-β equilibrium are overall more pressure-gradient-driven (compare figures 3*a* and 7*a*). Similarly to the ideal modes, the relative current-density drive strongly decreases with increasing toroidal mode number. Although the relative current-density drive is nearly independent of the resistivity, one can see that the perturbation and the corresponding energy densities are broadened with increasing resistivity (see figure 7*b*,*d*). We remark that the precise calculation of the energetic decomposition for the $n = 1$ mode is numerically challenging as the perturbation is finite at the magnetic axis, where the coordinate system is singular. For larger toroidal mode numbers, the resistive modes become increasingly localised at the $\iota = 1$ flux surface (see figure 7*d*). The pressure-gradient drive δW_{DP} strongly increases with increasing toroidal mode number, whereas the integrated current-density drive δW_{CUR} remains small because
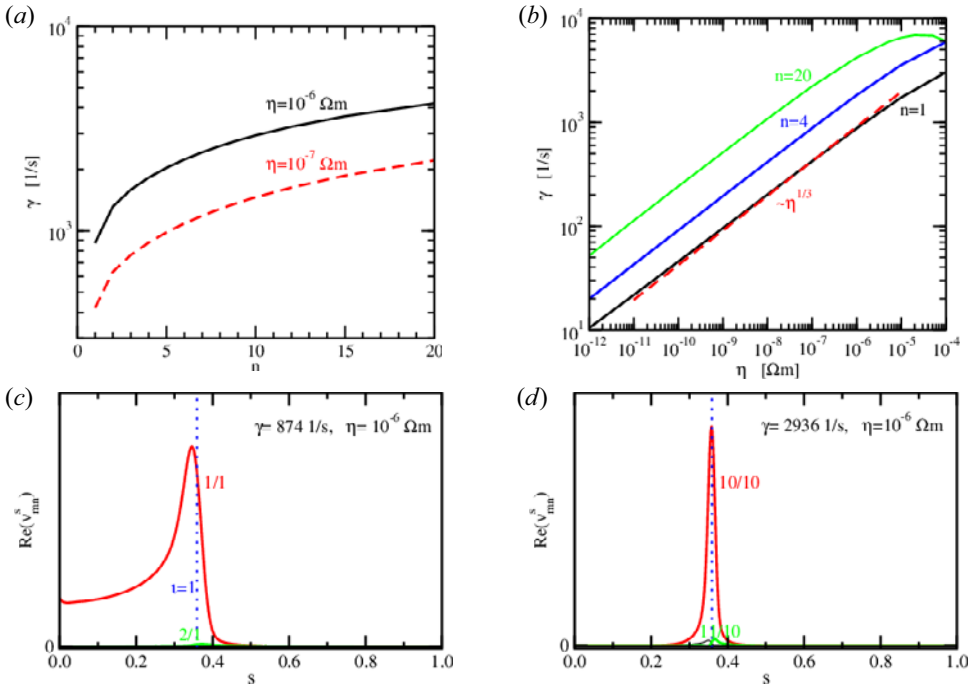
FIGURE 6. (*a*) Growth rates as functions of the toroidal mode number n for $\eta = 10^{-6}$ and $\eta = 10^{-7}\,\Omega\,\text{m}$. (*b*) Growth rates as functions of η for $n = 1$, 4 and 20. The red dashed line indicates the $\eta^{1/3}$ scaling. Fourier spectra of the real part of the radial velocity perturbation are shown for (*c*) an $n = 1$ and (*d*) an $n = 10$ mode. The blue dotted vertical lines indicate the position of the $\iota = 1$ rational flux surface.

of the cancellation of stabilising and destabilising contributions in different radial regions of the plasma (see figure 7*c*,*d*).

Figures 8 and 9 show growth rates and oscillation frequencies as functions of the parameter α_T and the toroidal mode number n, respectively. They include the limiting cases of cold ions ($\alpha_T = 0$) and cold electrons ($\alpha_T = 1$). In the case of cold ions, only the electron diamagnetic drift remains that is described by the parallel electron pressure-gradient term in the extended Ohm's law (2.11). In the case of cold electrons, only the ion diamagnetic drift influences the stability via the gyro-viscosity term in the momentum equation (2.9) and the perpendicular ion pressure-gradient term in (2.11). The comparison of the growth rates without (figure 6*a*) and with (figure 8*a*,*c*) diamagnetic drift effects shows a large stabilising effect for all combinations of ion and electron pressures. However, resistivity and electron temperature are coupled by the Spitzer resistivity in a real plasma. Using a rough estimate of the Spitzer resistivity, namely $\eta = 2.8 \times 10^{-8}/T_e^{3/2}\,\Omega\,\text{m}$ (T_e in keV, Coulomb logarithm $\ln \Lambda = 17$) (Wesson 1997), we obtain $T_e = 0.09$ and $T_e = 0.43\,\text{keV}$ for $\eta = 10^{-6}$ and $\eta = 10^{-7}\,\Omega\,\text{m}$, respectively. The corresponding α_T parameters are marked by the dotted vertical lines in figure 8. Cold ions ($\alpha_T = 0$) would correspond to an electron temperature of $T_e = 1\,\text{keV}$ and a small resistivity of $\eta = 2.8 \times 10^{-8}\,\Omega\,\text{m}$. Extrapolating the results presented in figures 8(*a*,*c*) and 9(*a*,*c*), we expect that, at least, all modes with $n > 1$ are stabilised by the electron diamagnetic drift effect. However, CASTOR3D computations show that also the $n = 1$ mode is stabilised for $\eta = 2.8 \times 10^{-8}\,\Omega\,\text{m}$ and $\alpha_T = 0$.
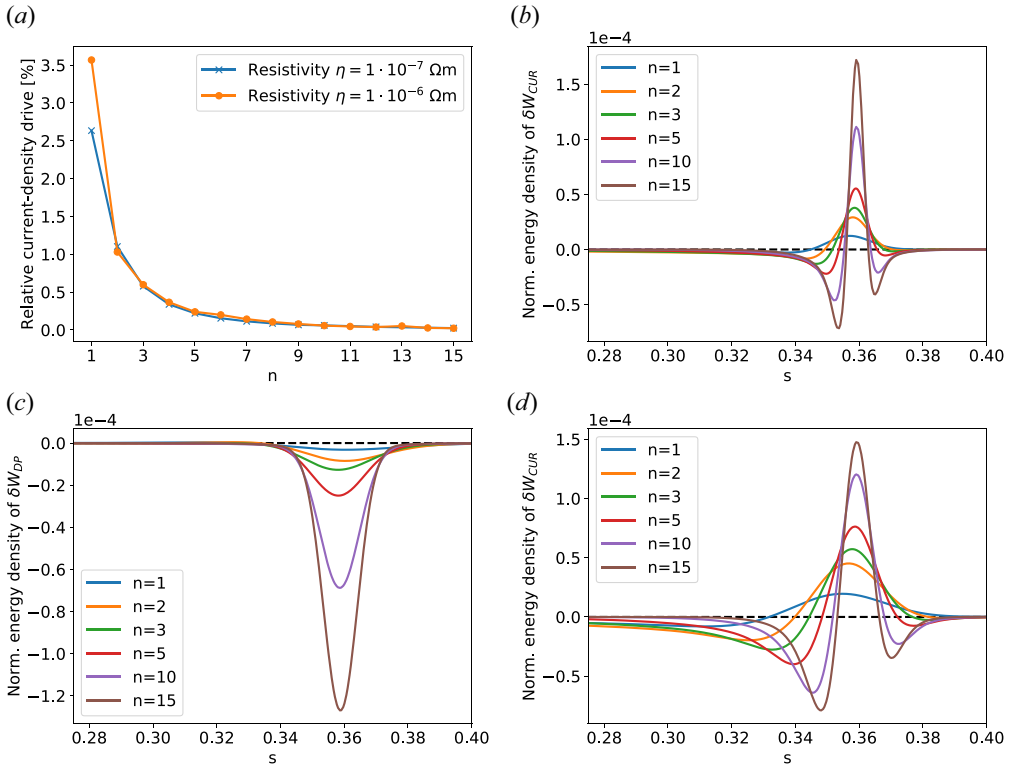
FIGURE 7. Energetic decomposition of the resistive internal perturbations of the considered low-beta equilibrium: (*a*) Relative current-density drive as a function of the toroidal mode number for resistivities of $\eta = 10^{-7}\,\Omega\,\mathrm{m}$ (blue) and $\eta = 10^{-6}\,\Omega\,\mathrm{m}$ (orange). Normalised energy densities corresponding to (*b,d*) the current-density and (*c*) the pressure-gradient drives as a function of the square root of the normalised toroidal flux for resistivities of (*b*) $\eta = 10^{-7}\,\Omega\,\mathrm{m}$ and (*c,d*) $\eta = 10^{-6}\,\Omega\,\mathrm{m}$.

The oscillation frequencies of the modes scale linearly with α_T (figure 8*b,d*) and n (figure 9*b,d*), at least for $\alpha_T > 0.2$. The deviation from the linear scaling is negligibly small and, therefore, would only be visible in an enlargement of the figures. The stars mark the ion diamagnetic drift frequencies for the corresponding toroidal mode numbers. These frequencies agree very well with the oscillation frequencies of the modes, that is, $\omega \approx \omega_i^*$, while $\omega \approx \omega_i^*/2$ holds for the ideal modes (see §3.1). Diamagnetic drift effects not only cause modes to oscillate in time, reduce growth rates or even stabilise modes, but may also make a less unstable mode to the most unstable one. The considered low-β equilibrium is unstable with respect to resistive kink and interchange modes (figures 8*c,d* and 10*a,c*), whose radial velocity perturbation (which is equivalent to the radial displacement) does not change its sign (no zero crossing). However, the equilibrium is also unstable to resistive modes whose radial velocity perturbation changes once its sign changes (one zero crossing) (figure 10*b,d*). The resistive energy functionals of the latter show a pressure-gradient drive of almost $100\,\%$, that is, the considered equilibrium is unstable with respect to a so-called Sturmian sequence of modes (Goedbloed & Sakanaka 1974). The considered modes with one zero crossing are mostly less unstable than the modes without zero crossing. However, in the case of cold electrons the resistive $n = 2$ mode with one zero crossing remains unstable, while the corresponding mode without
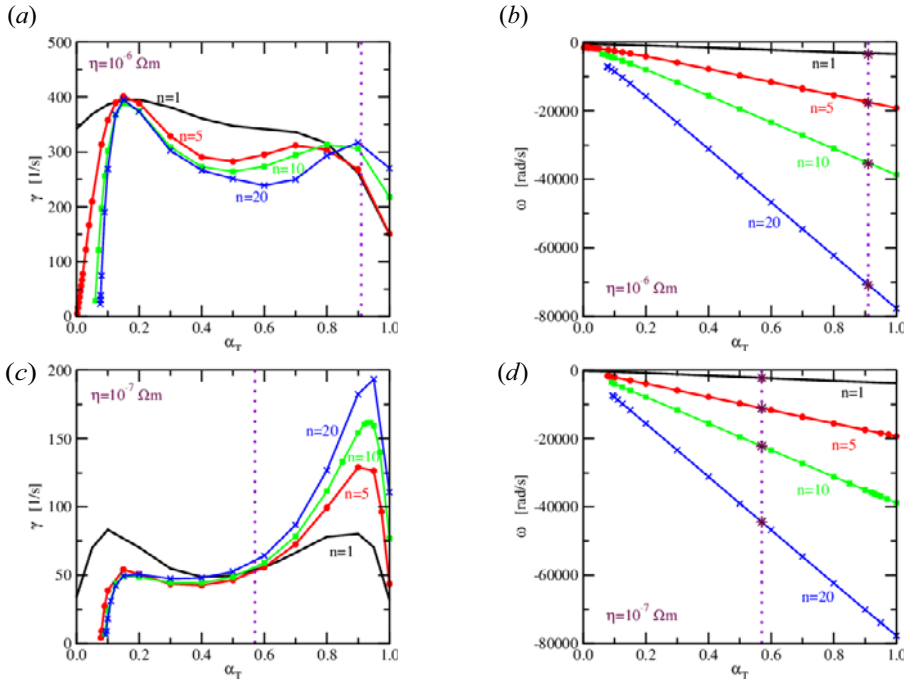
FIGURE 8. (*a,c*) Growth rates and (*b,d*) oscillation frequencies as functions of parameter α_T for various n. The dotted vertical lines mark the α_T values for which the considered resistivity value corresponds to the approximated Spitzer resistivity. The stars denote ω_i^*.

zero crossing is stabilised by the ion diamagnetic drift effect as shown in figure 9(*a,c*). There, the growth rates of both mode types are presented for $\alpha_T = 1$. In figure 10 the Fourier spectra of the real part of the radial velocity perturbation are presented for both $n = 3$ mode types without and with diamagnetic drift effects taken into account. Since the $n = 2$ mode without zero crossing is stable for $\alpha_T = 1$, the Fourier spectra are presented for the $n = 3$ modes which have analogous structures.

3.3. *Ideal stability studies (3-D equilibrium)*

The 3-D, stellarator-symmetric, high-β equilibrium differs from the previous considered up–down symmetric, axisymmetric equilibrium by an $n = 1$ helical core. Analogous to the axisymmetric one, this 3-D equilibrium is unstable with respect to ideal kink and interchange modes. Again, the ion diamagnetic drift effect taken into account by the gyro-viscosity term in the momentum equation (2.9) is the dominant effect, while the contributions of the pressure terms in Ohm's law (2.14) are negligibly small (see also Appendix B). However, particularly in 3-D geometry these drift terms cause additional numerical problems. That is, they increase the occurrence of non-physical 'parasitic' solutions, and lead to non-physical oscillations of the eigenfunctions. We therefore have neglected these terms in the following computations. Certainly, the pressure terms can only be neglected in Ohm's law in the case of highly unstable ideal modes (see § 3.1), but they play an essential role in the case of resistive modes as shown in § 3.2. The eigenvalue problem in general 3-D formulation yields two orthogonal solutions for an instability. The corresponding growth rates (real parts of the eigenvalues) are always equal (degenerate) for
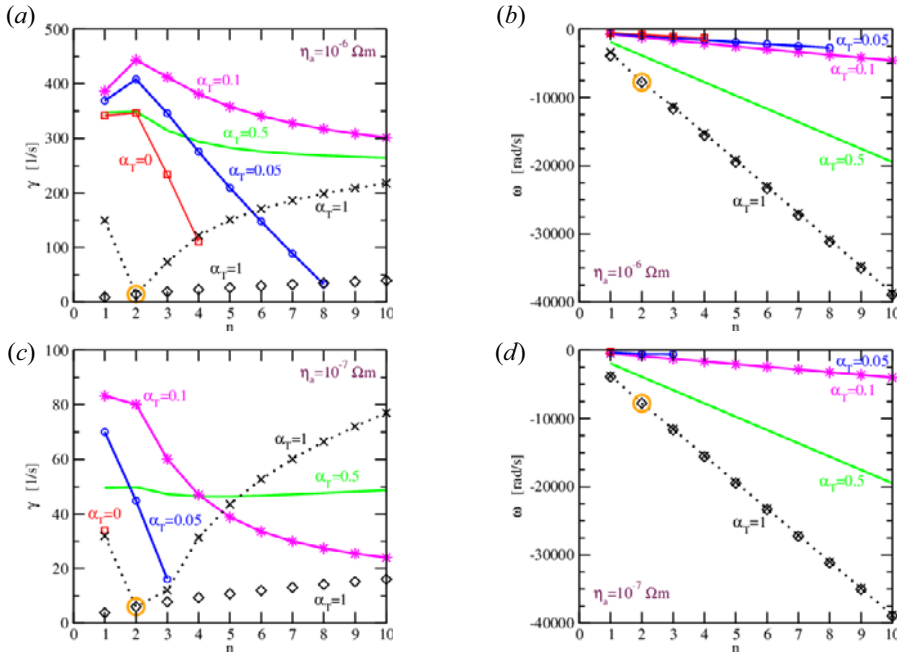
FIGURE 9. (*a,c*) Growth rates and (*b,d*) oscillation frequencies as functions of the toroidal mode number n for various α_T values: $\alpha_T = 0$ (red solid line with squares), $\alpha_T = 0.05$ (blue solid line with circles), $\alpha_T = 0.1$ (magenta solid line with plus symbols), $\alpha_T = 0.5$ (green solid line) and $\alpha_T = 1$ (resistive modes without zero crossing: black crosses; resistive modes with one zero crossing: black diamonds). The orange circle marks the change of the mode type.
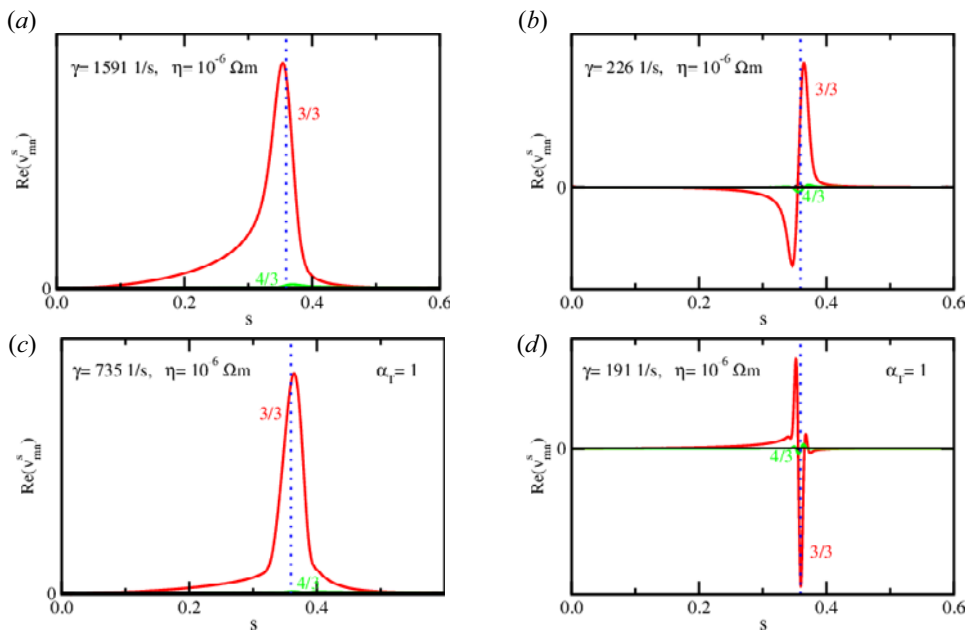

FIGURE 10. Fourier spectra of the real part of the radial velocity perturbations for (*a,c*) the resistive $n = 3$ mode without zero crossing and (*b,d*) the resistive $n = 3$ mode with one zero crossing (*a,b*) without and (*c,d*) with taking ion diamagnetic drift effects into account.
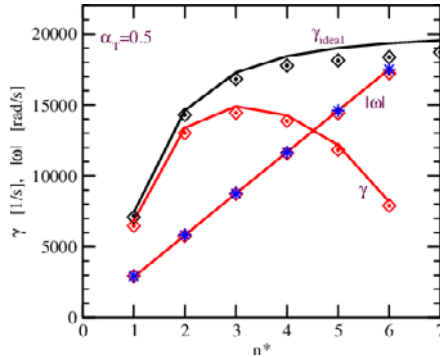
FIGURE 11. Growth rates γ and absolute values of the oscillation frequency $|\omega|$ as functions of n^* for the axisymmetric equilibrium (solid lines) and the 3-D equilibrium (dots and diamonds) with (red) and without (black) taking diamagnetic drift effects into account. The blue stars represent the absolute value of half of the ion diamagnetic drift frequency $|\omega_i^*|/2$.

axisymmetric configurations, but they may be different (non-degenerate) in the case of 3-D configurations. Finite oscillation frequencies (imaginary parts of the eigenvalues) always have the same absolute values, but opposite signs ($\omega_1 = -\omega_2$). However, those opposite signs do not mean that the corresponding modes rotate or oscillate contrarily. In fact, they rotate in the same direction as an illustration of the rotation in real space would show. In figure 11 the two growth rates of the instabilities are marked by dots and diamonds for the considered 3-D equilibrium. Here only the growth rates of the $n^* = 1$ internal kink mode without diamagnetic drift effects are slightly non-degenerate. We characterise the modes as n^*, because in 3-D geometry several n harmonics couple together and contribute to the Fourier spectrum of a mode, that is, n^* indicates the toroidal mode number of the global mode structure. As already mentioned in the introduction, in many cases n^* corresponds to the dominant toroidal Fourier harmonic contributing to the mode. In figure 13(*a,b*) the structures of the two solutions obtained without diamagnetic drift effects are shown for an $n^* = 1$ mode. They are orthogonal to each other, and they correspond to pure cosine (figure 13*a*) and sine (figure 13*b*) functions, because of the stellarator-symmetric equilibrium. In the case of an axisymmetric configuration the two structures would be equivalent, that is, one structure could be transformed into the other by multiplying the eigenfunctions with $e^{i\phi}$ (toroidal angle $\phi = \pm 90°$). Such a transformation is not possible in 3-D geometry. While, for the given example, the radial velocity perturbation (which in linear MHD is equivalent to the displacement of the mode) is perpendicular to the displacement of the helical core in figure 13(*a*), it is parallel in figure 13(*b*). These different locations result in the slightly unequal growth rates given in 13(*a,b*). (This small difference of the growth rates would only be well visible in an enlargement of figure 11.) The perturbation perpendicular to the helical core grows faster than the perturbation parallel to it. For a more detailed discussion of fast- and slow-growing solutions in 3-D tokamak configurations we refer the reader to Puchmayr *et al.* (2023). For completeness, it should also be mentioned that the complex linear eigenvalue problem, which is solved by the CASTOR3D code, can be multiplied with any complex number ($\neq 0$). That is, amplitudes and signs of the eigenfunctions are not determined.

In figure 11 the eigenvalues of the low-n^* modes are shown as a function of n^* with and without taking the ion diamagnetic drift effect into account, and assuming $\alpha_T = 0.5$. While without diamagnetic drift effects the $n^* = 1$ growth rates are appreciably non-degenerate
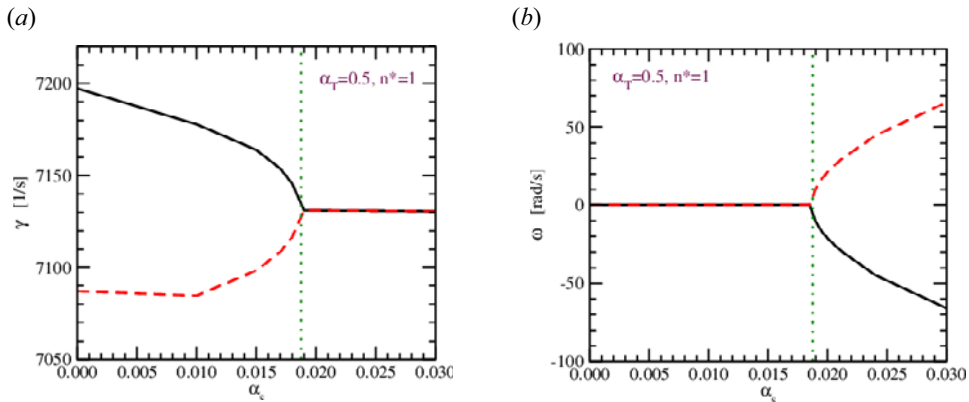
FIGURE 12. (*a*) Growth rates and (*b*) oscillation frequencies of the two possible $n^* = 1$ modes as functions of the scaling parameter α_s (enlargement of the interesting region). The green dotted lines ($\alpha_s = 0.01875$) mark the limit when the growth rates become degenerate and the modes start to oscillate.

(see also figure 12*a*), they become degenerate when taking those effects into account. As expected, the induced oscillation frequencies have opposite signs and equal absolute values. The latter agree to a good approximation with the high-β axisymmetric results and half the value of the ion diamagnetic drift frequency, $|\omega_i^*|/2$. Although the eigenvalues of the modes are very similar for the 3-D and the axisymmetric equilibria, there are two noteworthy differences between the two cases which we discuss in the following.

(a) If the growth rates of the two orthogonal solutions are different (non-degenerate) in the case without diamagnetic drift, a minimum strength of the diamagnetic drift effect (which corresponds to a minimum drift frequency) is necessary to equalise the growth rates and to start the mode oscillation. In figure 12 the growth rates and oscillation frequencies of the two possible $n^* = 1$ modes are shown as functions of the scaling parameter α_s. The initially non-degenerate growth rates converge until they become equal, while the modes start to oscillate ($\omega_1 = -\omega_2$). The opposite signs of the oscillation frequencies result in the same oscillation cycle, but are phase-shifted in time. An analogous behaviour has been observed with respect to plasma rotation in the case of external kink modes of a quasi-axisymmetric stellarator equilibrium (Strumberger & Günter 2019) and edge-localised modes in 3-D tokamak equilibria (Puchmayr *et al.* 2023). There, a minimum plasma rotation frequency is required for modes with non-degenerate growth rates to start oscillation. In figure 13 the vectors characterise the radial velocity perturbation in the R–Z plane at toroidal angle $\varphi = 0°$ and time $t = 0$ ($t = 0$ refers to the mode structure at the beginning of an oscillation cycle). Taking the ion diamagnetic drift effect into account, the structures are slightly rotated with respect to the location of the helical core.

(b) Diamagnetic drift effects change the Fourier composition of the eigenfunctions, as is illustrated for the $n^* = 6$ mode in figure 14. There, we only show the radial velocity perturbation of the cosine-type function (Fourier coefficients of the complex and complex conjugate eigenfunctions have the same sign and size), because the sine-type function (Fourier coefficients of the complex and complex conjugate eigenfunctions have opposite signs) yields no new information. (This also holds for the imaginary part of the Fourier coefficients.) Without diamagnetic drift effects the complex and complex conjugate components of the Fourier spectrum are equal (see figure 14*a*). However, with
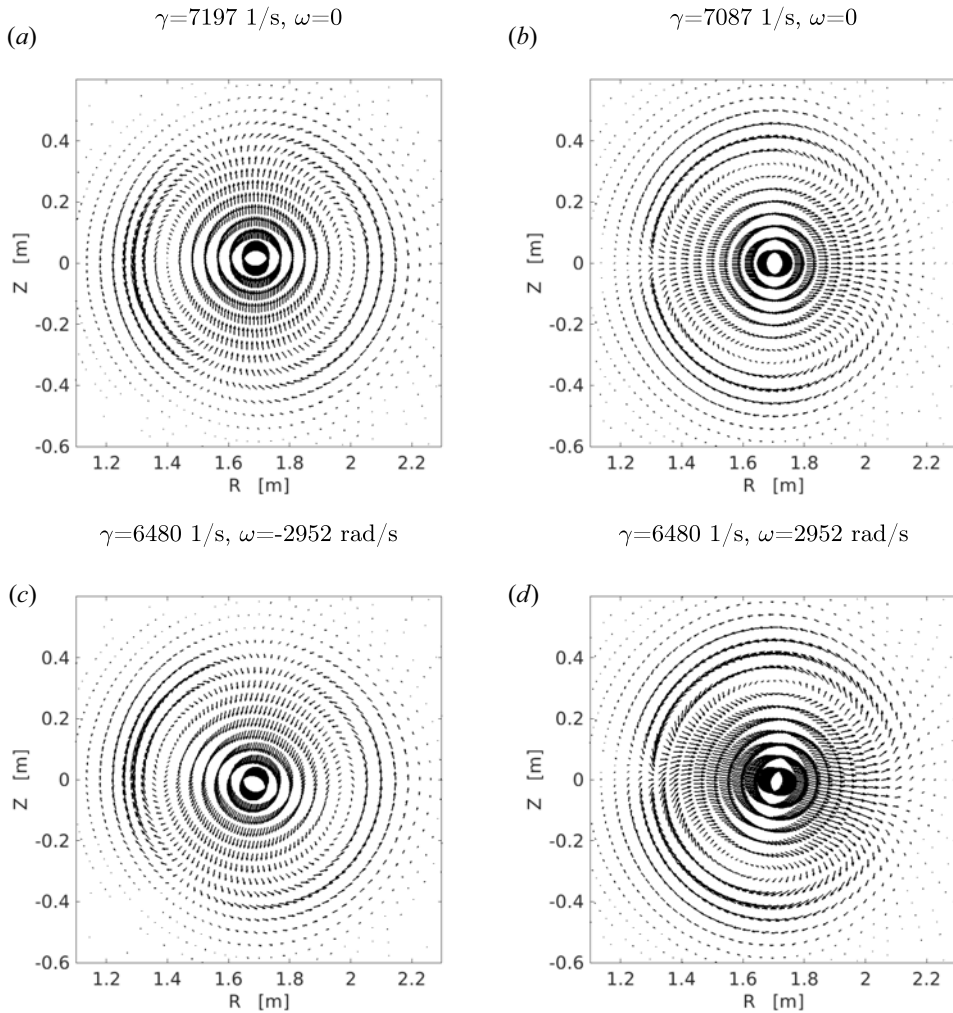
(a) $\gamma=7197\ 1/s,\ \omega=0$ (b) $\gamma=7087\ 1/s,\ \omega=0$

$\gamma=6480\ 1/s,\ \omega=-2952\ \mathrm{rad/s}$ $\gamma=6480\ 1/s,\ \omega=2952\ \mathrm{rad/s}$

(c) (d)

FIGURE 13. Structures of $n^* = 1$ mode for the two orthogonal solutions (a,b) without and (c,d) with taking the ion diamagnetic drift effect into account. The vectors characterise the velocity perturbation in the R–Z plane at toroidal angle $\varphi = 0°$ and time $t = 0$.

diamagnetic drift effects the complex or complex conjugate components strongly dominate the Fourier spectrum (figure 14b). It is not only the diamagnetic drift effects that cause such a decoupling of the complex and complex conjugate parts of the eigenfunctions. This decoupling has also been observed in the case of toroidal plasma rotation as described in Puchmayr *et al.* (2023). Besides, figure 14(a) illustrates the coupling of many toroidal harmonics. There, the dominant n cannot be identified. However, considering the perturbation in real space (see figure 14c), the $n^* = 6$ character of the mode appears. Taking diamagnetic drift effects into account, the toroidal coupling is reduced. The $m/n =$ 6/6 harmonic yields the largest contribution to the Fourier spectrum of the perturbation shown in figure 14(b), while the contributions of the other n harmonics are reduced. This reduction leads to a more uniformly distributed mode structure in the poloidal direction
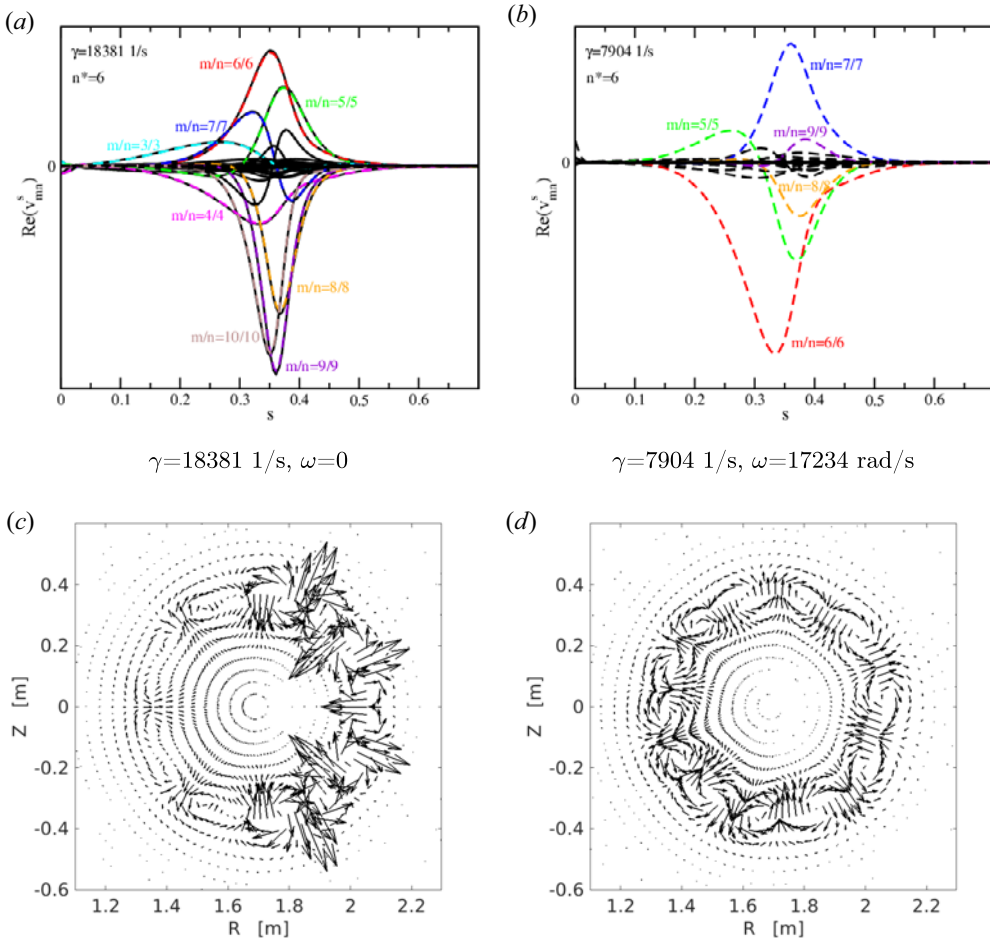
$\gamma{=}18381$ 1/s, $\omega{=}0$ $\gamma{=}7904$ 1/s, $\omega{=}17234$ rad/s

FIGURE 14. (a,b) Fourier spectra of the real part of the radial velocity perturbation and (c,d) mode structures of the $n^* = 6$ mode (a,c) without and (b,d) with ion diamagnetic drift effect. In (a,b) the solid and dashed lines denote the contributions of the complex and complex conjugate eigenfunctions, respectively. The largest contributions are marked by their poloidal and toroidal harmonics, m/n. In (c,d) the vectors characterise the velocity perturbation in the R–Z plane at toroidal angle $\varphi = 0°$ and time $t = 0$.

(see figure 14d). The coupling of the poloidal harmonics plays only a minor role for the mode structure, because of the very flat q-profile.

4. Summary and outlook

The 3-D linear resistive CASTOR3D code has been upgraded with respect to diamagnetic drift effects. The numerical results have been verified by comparing growth rates and oscillation frequencies computed with various coordinate types (see Appendix B). Furthermore, the presented results confirm previous findings (see e.g. Aiba 2016): (i) an ideal mode becomes stable when the absolute value of its oscillation frequency exceeds the corresponding ideal growth rate (the growth rate obtained without diamagnetic drift effects) and (ii) the oscillation frequency of an ideal mode agrees to a

good approximation with half of the absolute value of the corresponding ion diamagnetic drift frequency, that is, $\omega \approx \omega_i^*/2$.

Besides the standard approximations of equal pressures $p_i = p_e = 0.5p$ or cold ions $p_i = 0$, $p_e = p$, the CASTOR3D code allows any constant ratio of ion and electron pressures. The results show a strong dependence on this ratio. For ideal modes the stabilising diamagnetic drift effect decreases when the ion pressure is reduced, and is negligible for cold ions, because the ion diamagnetic drift effect is the major effect. In the case of resistive modes, however, both ion and electron diamagnetic drift effects are important. Their stabilising effects strongly depend on the ion/electron pressure ratio and the plasma resistivity. The oscillation frequencies of these modes agree very well with the corresponding ion diamagnetic drift frequencies, that is, $\omega \approx \omega_i^*$. Eventually, the type of the most unstable mode may change when diamagnetic drift effects are taken into account. The types of the modes have been specified by analysing the corresponding ideal or resistive energy functional that has been determined from the solution of the eigenvalue problem without diamagnetic drift effects.

Finally, the CASTOR3D code has been applied to a 3-D equilibrium, that is, a high-β equilibrium with helical core. These first results obtained for ideal kink and interchange modes confirm: (i) the growing stabilising diamagnetic drift effect with increasing toroidal mode number (which is the dominant toroidal harmonic n^*) and (ii) the oscillation frequencies of the modes correspond to a good approximation to $\omega_i^*/2$. Besides these similarities with the high-β axisymmetric equilibrium, additional effects have been found, namely: (i) sufficiently strong diamagnetic drift effects lead to a degeneration of otherwise non-degenerate growth rates, (ii) only modes with degenerate growth rates are able to oscillate and (iii) the diamagnetic drift effects change the composition of the eigenfunctions, that is, either the complex or the complex conjugate parts dominate the Fourier spectrum of the mode, and also the coupling of the toroidal harmonics is reduced leading to an alteration of the mode structure.

While here simple test equilibria have been investigated to demonstrate the reliability of the CASTOR3D code, the code will be applied to realistic tokamak and stellarator equilibria next. Diamagnetic drift effects are, for example, of particular importance for MHD instabilities located in the pedestal region of H-mode plasmas (ELM stability). For this reason, an important application of the extended CASTOR3D code will be an investigation of how 3-D magnetic fields produced by magnetic perturbation coils, which are used for ELM control, change the linear MHD stability limits.

Acknowledgements

Funding

Declaration of interests

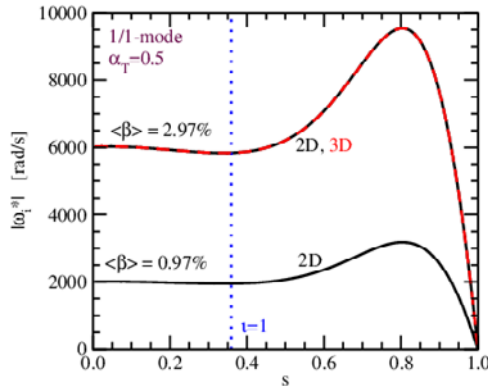The authors report no conflict of interest.

FIGURE 15. Ion diamagnetic drift frequency as a function of the square root of the normalised toroidal flux s for a 1/1 mode and two volume-averaged β-values: $\langle\beta\rangle = 2.96\%$ (black solid line: 2-D equilibrium; red dashed line: 3-D equilibrium) and $\langle\beta\rangle = 0.97\%$ (black solid line). The dotted vertical line marks the position of the $\iota = 1$ flux surface.

Appendix A. Ion diamagnetic drift frequency

The ion diamagnetic drift frequency $\omega_i^* = \boldsymbol{V}_i^* \cdot \boldsymbol{k}$ ($\boldsymbol{k}$ is wavenumber vector) is a useful quantity for the discussion of diamagnetic drift effects. In Boozer coordinates (s, v, u) the contravariant toroidal V_i^{*v} and poloidal V_i^{*u} components of the ion drift velocity

$$
\begin{aligned}
V_i^* &= \frac{m_i}{e} \frac{1}{\rho} \frac{\boldsymbol{B} \times \boldsymbol{\nabla} p_i}{B^2} \\
&= \frac{m_i}{e} \frac{1}{\rho} \frac{\partial p_i}{\partial s} \left(\frac{I}{\Phi' J + \Psi' I} \boldsymbol{r}_{,v} - \frac{J}{\Phi' J + \Psi' I} \mathbf{r}_{,u} \right) = V_i^{*v} \boldsymbol{r}_{,v} + V_i^{*u} \boldsymbol{r}_{,u}
\end{aligned}
\tag{A1}
$$

are constant on flux surfaces, because ion pressure p_i, mass density ρ, poloidal current J, toroidal current I and the derivatives of poloidal flux Ψ' and toroidal flux Φ' depend only on the radial flux coordinate s. We approximate $\boldsymbol{k}$ by $\boldsymbol{k} = -\mathrm{i}(\boldsymbol{\nabla} f / f)$, with function $f = f_0(s) \exp(2\pi\mathrm{i}(mu - nv))$. The latter describes the perturbation by the leading m, n Fourier harmonics. Then, we obtain for the ion diamagnetic drift frequency

$$
\omega_i^* = 2\pi (m V_i^{*u} - n V_i^{*v}).
\tag{A2}
$$

Applying (A2) to the 1/1 modes of the high- and low-β test equilibria, we get the ion diamagnetic drift frequencies shown in figure 15. There, we assumed $p_i = p_e$, that is, $\alpha_T = 0.5$. The resulting absolute values of the ion diamagnetic drift frequencies amount to $|\omega_i^*| = 5841 \,\mathrm{rad\,s^{-1}}$ (high-β case) and $|\omega_i^*| = 1947 \,\mathrm{rad\,s^{-1}}$ (low-β case) at the $\iota = 1$ flux surface. There is no visible difference between the drift frequencies of the 2-D and 3-D high-β equilibria, because of the identical profiles and the small deviations between 2-D and 3-D flux surfaces. (Here the ion diamagnetic drift frequency is negative because of the used orientation of the magnetic field.)

Appendix B. Numerical accuracy

The CASTOR3D code uses nested, non-orthogonal 3-D flux coordinates (Strumberger & Günter 2017). Its general formulation allows the use of various coordinate types (e.g. NEMEC coordinates (Hirshman & Whitson 1983), Boozer coordinates (Boozer 1982) and 2-D straight field line coordinates (Huysmans *et al.* 1993)). The latter are limited
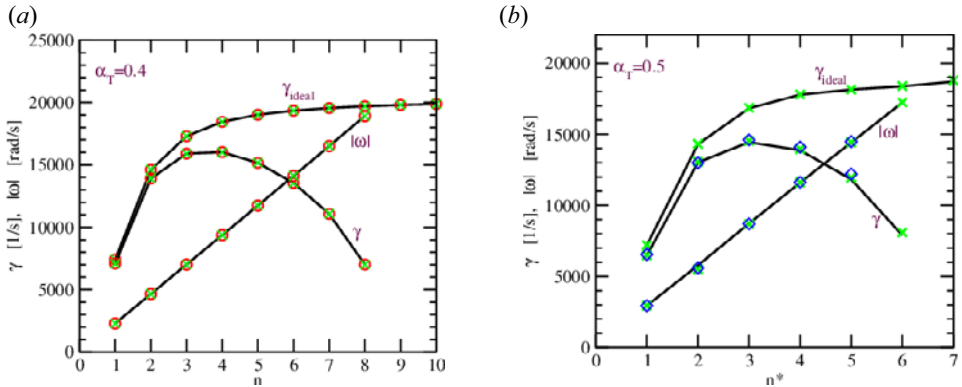
FIGURE 16. Growth rate γ and absolute value of the oscillation frequency $|\omega|$ of the ideal modes as functions of the toroidal mode number n for (*a*) 2-D equilibrium, $\alpha_T = 0.4$, and (*b*) 3-D equilibrium, $\alpha_T = 0.5$ (NEMEC flux coordinates: black solid lines; Boozer coordinates: green crosses; 2-D straight field line coordinates: red circles). Here γ_{ideal} is the growth rate without taking diamagnetic drift effects into account. (*a*) Growth rate γ and $|\omega|$ with ion and electron diamagnetic drift effects and (*b*) γ and $|\omega|$ only with ion diamagnetic drift effect (black solid lines, green crosses) and with both effects (NEMEC coordinates: blue diamonds).

to axisymmetric equilibria. Using different coordinate types, errors in the formulation and/or implementation of the matrix elements, as well as a non-sufficient radial resolution or an unsuitable Fourier spectrum will lead to differing results. We therefore performed convergence studies with respect to Fourier spectra and radial grid resolutions for these three coordinate types and compared the results, in order to find the most appropriate ones.

Figures 16 and 17 show the almost perfect agreement of growth rates and oscillation frequencies obtained for ideal and resistive modes. Of course, only NEMEC and Boozer coordinates have been used in the case of the 3-D equilibrium (figure 16*b*). Concerning memory and computational time, 3-D calculations are much more expensive than 2-D calculations because of the toroidal mode coupling. Furthermore, they are more sensitive to numerical inaccuracies, so that non-physical 'parasitic' solutions and non-physical oscillations of the eigenfunctions increase with every physical effect that is additionally taken into account. Therefore, the computations presented in § 3.3 are restricted to the ion diamagnetic drift effect taken into account by the gyro-viscosity. Using NEMEC coordinates, however, we have been able to find several solutions taking ion and electron diamagnetic drift effects into account simultaneously. These results are additionally shown in figure 16(*b*). They confirm that neglecting the pressure terms in Ohm's law (2.14) is justified for the considered high-β equilibrium.

There are several criteria to distinguish between non-physical and physical solutions. (a) Viewing the Fourier spectra of all perturbed quantities. In the case of non-physical solutions all Fourier spectra oscillate irregularly. (b) Making a scan over physical parameters (e.g. resistivity, toroidal mode number, etc.). The eigenvalues of non-physical solutions usually yield no smooth curves. (c) Making a scan over numerical parameters (e.g. number of radial grid points, number of Fourier harmonics, etc.). The eigenvalues of 'parasitic' solutions do not in general converge. They strongly depend on numerical parameters. (d) Using different coordinate types. Sometimes, a coordinate type produces more non-physical solutions than another one. While, ideally, physical solutions have almost identical eigenvalues in different coordinate systems (see figures 16 and 17), the
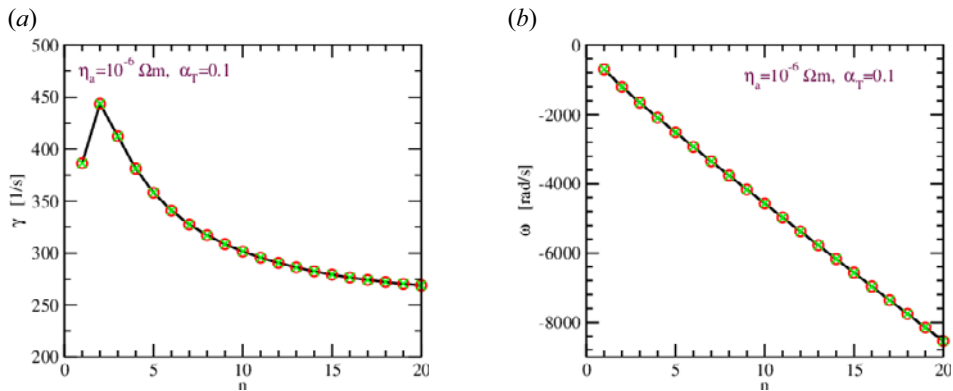
FIGURE 17. (*a*) Growth rate and (*b*) oscillation frequency as functions of the toroidal mode number (NEMEC flux coordinates: black solid line; straight field line coordinates: red circles; Boozer coordinates: green crosses) of the resistive modes with ion and electron diamagnetic drift effects.

'parasitic' eigenvalues can usually not be reproduced with other coordinates. Together, these criteria allow one to identify the 'parasitic' solutions in most cases.

REFERENCES

AIBA, N. 2016 Impact of ion diamagnetic drift on ideal ballooning mode stability in rotating tokamak plasmas. *Plasma Phys. Control. Fusion* **58** (4), 045020.

ANDERSON, D.V., COOPER, W.A., GRUBER, R., MERAZZI, S. & SCHWENN, U. 1990 Methods for the efficient calclation of the (MHD) magnetohydrodynamic stability properties of magnetically confined fusion plasmas. *Intl J. Supercomput. Appl*. **4**, 34.

BOOZER, A.H. 1982 Establishment of magnetic coordinates for a given magnetic field. *Phys. Fluids* **25**, 520.

BRAGINSKII, S.I. 1965 Transport processes in a plasma. In *Reviews of Plasma Physics* (ed. M.A. Leontovich), vol. 1, p. 205. Consultants Bureau.

CHANG, Z. & CALLEN, J.D. 1992 Unified fluid/kinetic description of plasma microinstabilities. Part 1. Basic equations in a sheared slab geometry. *Phys. Fluids* B **4**, 1167–1181.

CHAPMAN, I. T., SHARAPOV, S.E., HUYSMANS, G. T.A. & MIKHAILOVSKII, A.B. 2006 Modelling the effect of toroidal plasma rotation on drift-magnetohydrodynamic modes in tokamaks. *Phys. Plasmas* **13** (6), 062511.

CHU, M.S., GREENE, J.M., JENSEN, T.H., MILLER, R.L., BONDESON, A., JOHNSON, R.W. & MAUEL, M.E. 1995 Effect of toroidal plasma flow and flow shear on global magnetohyrdodynamic MHD modes. *Phys. Plasmas* **2**, 2236.

GOEDBLOED, J.P. & SAKANAKA, P.H. 1974 New qpproach to magnetohydrodynamic stability: I. A practical stability concept. *Phys. Fluids* **17**, 908.

HIRSHMAN, S.P., VAN RIJ, W.I. & MERKEL, P. 1986 Three-dimensional free boundary calculations using a spectral Greens's function method. *Comput. Phys. Commun*. **43** (1), 143.

HIRSHMAN, S.P. & WHITSON, J.C. 1983 Steepest-decent moment method for three-dimensional magnetohydrodynamic equilibria. *Phys. Fluids* **26** (12), 3553.

HOELZL, M., HUIJSMANS, G.T.A., PAMELA, S.J.P., BÉCOULET, M., NARDON, E., ARTOLA, F.J., NKONGA, B., ATANASIU, C.V., BANDARU, V., BHOLE, A., *et al.* 2021 The JOREK non-linear extended MHD code and applications to large-scale instabilities and their control in magnetically confined fusion plasmas. *Nucl. Fusion* **61** (6), 065001.

HUYSMANS, G.T.A., GOEDBLOED, J.P. & KERNER, W. 1993 Free boundary resistive modes in tokamaks. *Phys. Fluids* B **5**, 1545.

HUYSMANS, G.T.A., SHARAPOV, S.E., MIKHAILOVSKII, A.B. & KERNER, W. 2001 Modeling of diamagnetic stabilization of ideal magnetohydrodynamic instabilities associated with the transport barrier. *Phys. Plasmas* **8**, 4292.

LÜTJENS, H. & LUCIANI, J.-F. 2010 XTOR-2F: a fully implicit Newton–Krylov solver applied to nonlinear 3D extended MHD in tokamaks. *J. Comput. Phys.* **229** (21), 8130–8143.

MIKHAILOVSKII, A.B. 1998 Generalized MHD for numerical stability analysis of high-performance plasmas in tokamaks. *Plasma Phys. Control. Fusion* **40** (11), 1907.

NÜHRENBERG, C. 1996 Global ideal magnetohydrodynamic stability analysis for the configurational space of Wendelstein 7–X. *Phys. Plasmas* **3** (6), 2401–2410.

PAMELA, S.J.P., BHOLE, A., HUIJSMANS, G.T.A., NKONGA, B., HOELZL, M., KREBS, I. & STRUMBERGER, E. 2020 Extended full-MHD simulation of non-linear instabilities in tokamak plasmas. *Phys. Plasmas* **27** (10), 102510.

PUCHMAYR, J., DUNNE, M. & STRUMBERGER, E. 2022 An intuitive form of the energy functional for resistive plasma perturbations. *J. Plasma Phys.* **88** (5), 905880512.

PUCHMAYR, J., DUNNE, M., STRUMBERGER, E., WILLENSDORFER, M., ZOHM, H., HINDENLANG, F. & THE ASDEX UPGRADE TEAM 2023 Helical mode localization and mode locking of idea MHD instabilities in magnetically perturbed tokamak plasmas. *Nuclear Fusion* (submitted).

SCHNACK, D.D., BARNES, D.C., BRENNAN, D.P., HEGNA, C.C., HELD, E., KIM, C.C., KRUGER, S.E., PANKIN, A.Y. & SOVINEC, C.R. 2006 Computational modeling of fully ionized magnetized plasmas using the fluid approximation. *Phys. Plasmas* **13**, 058103.

STRUMBERGER, E. & GÜNTER, S. 2017 CASTOR3D: linear stability studies for 2D and 3D tokamak equilibria. *Nucl. Fusion* **57** (1), 016032.

STRUMBERGER, E. & GÜNTER, S. 2019 Linear stability studies for a quasi-axisymmetric stellarator configuration including effects of parallel viscosity, plasma flow, and resistive walls. *Nucl. Fusion* **59** (10), 106008.

WESSON, J. 1997 Plasma physics. In *Tokamaks*, 2nd edn, chap. 2. Clarendon Press.

YU, Q., GÜNTER, S. & SCOTT, B.D. 2003 Numerical modeling of linear drift-tearing mode stability. *Phys. Plasmas* **10**, 707.